Chapter 1

Introduction

1.1 Optics at the Nanoscale

The interaction of light with matter is one of the most significant processes on the planet, forming the basis of some of the most famous scientific discoveries to date. However, since its inception more than four hundred years ago, any advances in the field of optics have been limited by diffraction. This restricts the size of all optical components to dimensions greater than half the wavelength of light it supports [1]. It has only been in the past decade that researchers have finally developed a technology that beats the diffraction limit, instigating a revolution in optics. Plasmonics is an emerging area of research that opens the path for controlling light-matter interactions on the subwavelength scale, enabling truly nanophotonic technologies that are unattainable with conventional diffraction-limited optical components. Novel surface plasmon devices exploit electromagnetic waves confined to the interface between a metal and a dielectric and permit the researcher to "shrink" light to dimensions previously inaccessible with optics.

Although scientists take credit for revolutionizing this field fairly recently, in truth nanophotonics, and specifically plasmonics, has been in practical applications since the 4th century. Figure 1.1a shows a photograph of the Lycurgus cup from 4th century Rome, which consists of metallic nanoparticles suspended within a glass matrix. Because of plasmonic excitation of electrons in the metallic particles, the cup absorbs and scatters the short wavelengths of the visible spectrum, blue and green light. Therefore, when viewed in reflection, the plasmonic scattering gives the cup a greenish hue. If instead a white light source is placed within the goblet, the metal
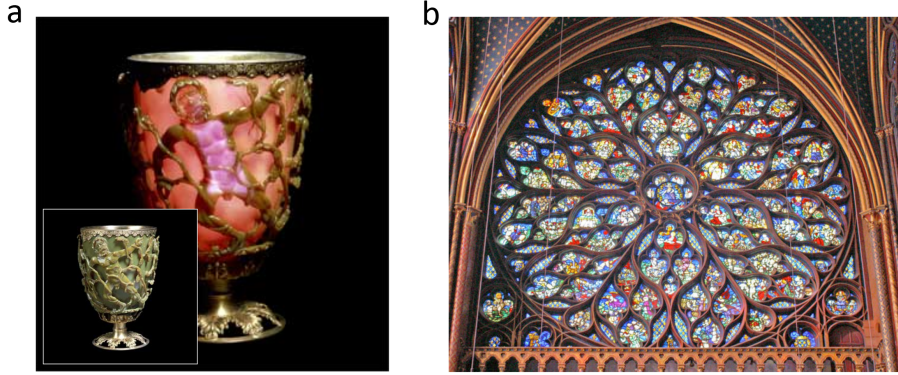
Figure 1.1. (a) The Lycurgus cup from 4th century Rome consists of small metal nanoparticles suspended within the glass matrix. Because of plasmonic excitation of electrons in the metallic particles, the plasmonic scattering in reflection gives the cup a greenish hue (inset). If a white light source is placed within the goblet, the glass appears red because it transmits only the longer wavelengths of the visible spectrum and absorbs the shorter ones (image from [2]). (b) The famous Rose window in Sainte Chapelle (12th century Paris) has its brilliant colors because of a similar phenomenon (image by B. Didier).

nanoparticles in the glass transmit the longer wavelengths of the visible spctrum and absorb the shorter ones, and the cup appears red. The brilliant colors in the famous stained-glass Rose window of Sainte Chapelle in 12th century Paris (Figure 1.1b) are created using this same technique, as the scattering and transmissive properties of metal nanoparticles are strongly shape and size dependent.

1.2 What are Surface Plasmons?

Surface plasmons are longitudinal charge-density fluctuations at the interface between a metal and a dielectric [3]. They resemble photons, but are nonradiative in nature and generally exhibit much shorter wavelengths than photons in free space. Surface plasmons essentially exist in two forms, as *localized* surface plasmons (SPs) and as
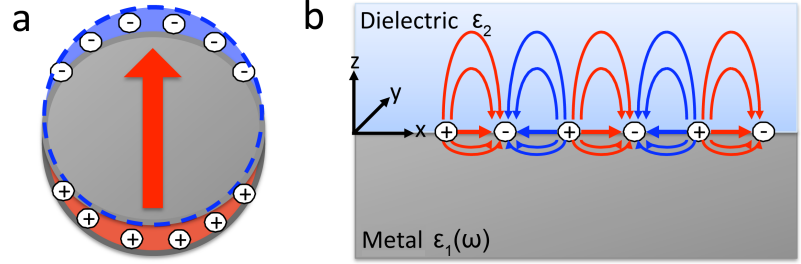
Figure 1.2. (a) Example of a particle plasmon. An incident electromagnetic field causes a disturbance of the electron cloud in the particle (negative charges), leaving behind a positively charged portion of the particle. The electron cloud then oscillates at the dipole plasmon resonance frequency. (b) Surface plasmons are also supported at the planar interface between a dielectric (ε_2) and a metal ($\varepsilon_1(\omega)$). Here, an incident field excites a charge-compression wave that propagates along the metal/dielectric interface.

propagating surface plasmon polaritons (SPPs). An example of localized SPs are those supported by metal nanoparticles, illustrated schematically in Figure 1.2a. In this case, an incident electromagnetic field causes the electron cloud in the nanoparticle to oscillate coherently, resulting in positive and negative charge polarization. A restoring force arises from the Coulomb attraction between the displaced electrons and the positively charged nuclei, and the electron cloud oscillates at the dipolar plasmon resonance frequency [4]. These nanoparticles find applications in surface enhanced Raman spectroscopy [5, 6, 7], photothermal tumor ablation [8], and enhanced absorption in solar cells (see [9] and references therein), among others. In planar geometries, surface plasmons propagate as a longitudinal charge-compression wave at the interface of a metal and dielectric. As illustrated in Figure 1.2b, the field penetrates more significantly into the dielectric half-space than the metal, although both of these distances can be subwavelength.

1.3 Single-Interface Surface Plasmons

In this section, we will derive the single-interface surface plasmon dispersion relation [10]. We start with Maxwell's equations, which describe macroscopic electromagnetism:

$$\nabla \cdot \mathbf{D} = \rho_{\text{ext}} \tag{1.1a}$$

$$\nabla \cdot \mathbf{B} = 0 \tag{1.1b}$$

$$\nabla \times \mathbf{E} = -\frac{\partial \mathbf{B}}{\partial t} \tag{1.1c}$$

$$\nabla \times \mathbf{H} = \mathbf{J_{ext}} + \frac{\partial \mathbf{D}}{\partial t}. \tag{1.1d}$$

These equations relate the fields $\mathbf{D}$ (dielectric displacement), $\mathbf{E}$ (electric field), $\mathbf{B}$ (magnetic induction), and $\mathbf{H}$ (magnetic field) to ρ_{ext} (external charge density) and $\mathbf{J_{ext}}$ (external current density). Limiting ourselves to isotropic, linear, nonmagnetic media, we also have

$$\mathbf{D} = \varepsilon_0 \varepsilon \mathbf{E} \tag{1.2a}$$

$$\mathbf{B} = \mu_0 \mu \mathbf{H}, \tag{1.2b}$$

where ε_0 and μ_0 are the electric permittivity and magnetic permeability, respectively, ε is the dielectric constant (relative permittivity), and $\mu = 1$ defines the relative permeability of nonmagnetic media.

Combining (1.1c) and (1.1d), we can derive the wave equation,

$$\nabla \times \nabla \times \mathbf{E} = -\mu_0 \frac{\partial^2 \mathbf{D}}{\partial t^2}, \tag{1.3}$$

the basis of electromagnetic wave theory. If we assume harmonic time dependence $\mathbf{E}(\mathbf{r}, t) = \mathbf{E}(\mathbf{r}) e^{-i\omega t}$, (1.3) simplifies to its more familiar form as the Helmholtz equation,

$$\nabla^2 \mathbf{E} + k_0^2 \varepsilon \mathbf{E} = 0, \tag{1.4}$$

where $k_0 = \omega/c$ is the wave vector of the propagating wave in vacuum, ω is frequency, and c is the speed of light in vacuum.

To find a solution to the Helmholtz equation, we assume a one-dimensional geometry with propagation in the $+x$ direction along the interface $z = 0$, as seen in Figure 1.2b. Thus, the functional form of our solution is

$$\mathbf{E}(x, y, z, t) = \mathbf{E}(z)e^{\imath\beta x}e^{-\imath\omega t}, \tag{1.5}$$

where $\beta = k_x$ is the propagation constant. Plugging this into (1.4) gives the desired form of the wave equation,

$$\frac{\partial^2 \mathbf{E}(z)}{\partial z^2} + \left(k_0^2 \varepsilon - \beta^2\right)\mathbf{E} = 0, \tag{1.6}$$

with a similar expression for the magnetic field $\mathbf{H}$. To solve for the spatial field profile and dispersion relation of propagating waves, we seek specific expressions for $\mathbf{E}$ and $\mathbf{H}$. These waves propagate at the interface between a conducting half-space ($z < 0$) with complex dielectric function $\varepsilon_1(\omega)$, and a non-absorbing half-space ($z > 0$) of dielectric material with real dielectric constant ε_2 (Figure 1.2b). For metals, this implies $\mathrm{Re}[\varepsilon_1] < 0$, which is satisfied at frequencies below the plasma frequency ω_p. We also expect this propagating wave at the metal-dielectric interface to decay evanescently into both media.

Plugging (1.5) into Maxwell's equations, we find two sets of solutions with differing polarizations. The first are transverse magnetic (TM) solutions where the only non-zero field components are E_x, E_z, and H_y. In this case, we find for $z > 0$ (in the dielectric),

$$H_y(z) = A_2 e^{\imath\beta x}e^{-k_2 z} \tag{1.7a}$$

$$E_x(z) = \imath A_2 \frac{1}{\omega\varepsilon_0\varepsilon_2}k_2 e^{\imath\beta x}e^{-k_2 z} \tag{1.7b}$$

$$E_z(z) = -A_1 \frac{\beta}{\omega\varepsilon_0\varepsilon_2}e^{\imath\beta x}e^{-k_2 z} \tag{1.7c}$$

and for $z < 0$ (in the metal),

$$H_y(z) = A_1 e^{\imath\beta x} e^{k_1 z} \tag{1.8a}$$

$$E_x(z) = -\imath A_1 \frac{1}{\omega\varepsilon_0\varepsilon_1} k_1 e^{\imath\beta x} e^{k_1 z} \tag{1.8b}$$

$$E_z(z) = -A_1 \frac{\beta}{\omega\varepsilon_0\varepsilon_1} e^{\imath\beta x} e^{k_1 z}, \tag{1.8c}$$

where $k_i \equiv k_{z,i}$, is the z component of the wave vector in media $i = 1$ (metal) and $i = 2$ (dielectric). Applying boundary conditions requiring continuity of H_y and $\varepsilon_i E_z$ at the interface, we find that $A_1 = A_2$ and $k_2/k_1 = -\varepsilon_2/\varepsilon_1$. Also solving the wave equation for H_y gives

$$k_1^2 = \beta^2 - k_0^2\varepsilon_1 \tag{1.9a}$$

$$k_2^2 = \beta^2 - k_0^2\varepsilon_2. \tag{1.9b}$$

Finally, this gives us the dispersion relation:

$$\beta = k_0\sqrt{\frac{\varepsilon_1\varepsilon_2}{\varepsilon_1 + \varepsilon_2}}. \tag{1.10}$$

If we also seek transverse electric (TE) modes, where H_x, H_z, and E_y are the only non-zero field components, we find that no surface modes confined to the interface can exist with this polarization. Thus, SPPs only exist for TM polarization.

Reexamining the dispersion relation of (1.10), we see that there is a resonant condition when $\varepsilon_1(\omega) = -\varepsilon_2$, satisfied at the surface plasmon resonance,

$$\omega_{\mathrm{sp}} = \frac{\omega_{\mathrm{p}}}{\sqrt{1 + \varepsilon_2}}, \tag{1.11}$$

where ω_{sp} is the surface plasmon resonance frequency and ω_{p} is the bulk plasma frequency of the metal. The surface plasmon dispersion relation for Ag/air is plotted in Figure 1.3 as energy ($\hbar\omega$) versus k_x. The light line (LL) in air is plotted in gray ($E = \hbar\omega = \hbar c k_x$). For energies below the surface plasmon resonance, the
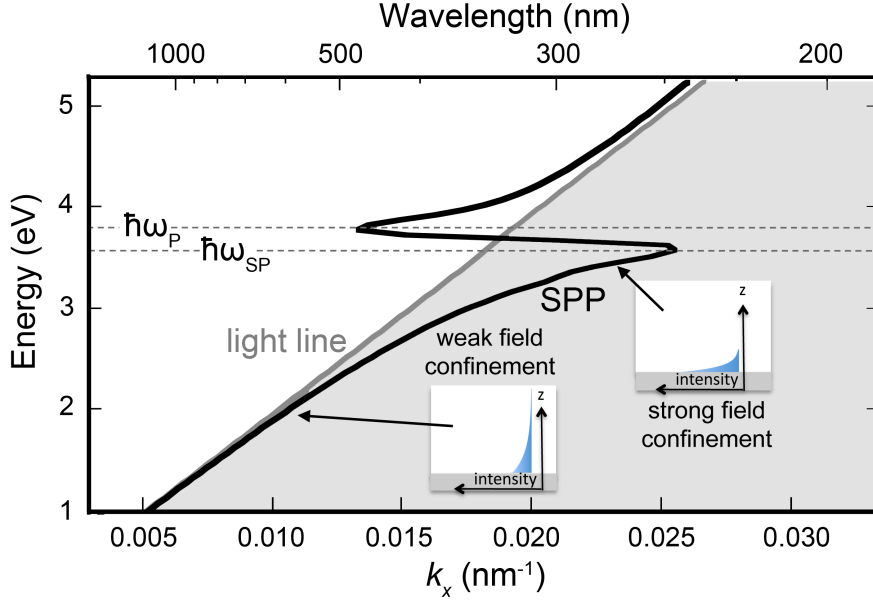
6

Figure 1.3. Dispersion relation for a single-interface (Ag/air) SPP, as in (1.10). The light line (LL) is plotted in gray, and the SPP dispersion in black. The light gray shaded region to the right of the LL indicates bound surface modes ($E < \hbar\omega_{\mathrm{sp}}$), while the region to the left of the LL holds radiative modes ($E > \hbar\omega_{\mathrm{p}}$). The inset images show that near the surface plasmon resonance ($\hbar\omega_{\mathrm{sp}}$), fields are highly localized at the metal/dielectric interface in the z direction (strong field confinement). At lower energies when the SPP dispersion lies closer to the LL, fields penetrate more significantly into the dielectric environment (weak field confinement).

SPP dispersion lies to the right of the LL. Thus, at a given free-space energy, the SPP accesses larger k-vectors, or shorter wavelengths $\lambda = 2\pi/k_x$, than its free-space counterpart. This effect becomes more pronounced nearer to the surface plasmon resonance. Because of this so-called momentum mismatch, photons in free space cannot directly excite SPPs. Several strategies have been developed to overcome this, such as those mentioned in Section 1.4. Also shown in Figure 1.3 are schematics of the field penetration into the dielectric (air) for different regions of the dispersion diagram. At low energies when the SPP dispersion lies very close to the light line, there is weak field confinement in the z direction. Approaching resonance, the fields are more tightly confined to the Ag/air interface with higher field intensity as well.

Above the bulk plasma frequency ($E > \hbar\omega_{\mathrm{p}}$), when the metal becomes transparent, modes are no longer bound to the interface and are instead radiative modes, and between the bulk plasma resonance and the surface plasmon resonance are the quasi-bound modes [11]. We can also calculate the propagation length of the SPPs along the metal/dielectric interface. The fields depend on x as $\mathrm{e}^{\iota\beta x}$, so we define the propagation distance L_{SPP} as

$$L_{\mathrm{SPP}} = \frac{2}{\mathrm{Re}[\iota\beta]} = \frac{2}{\mathrm{Im}[\beta]}. \tag{1.12}$$

If we consider a planar multilayer system consisting of not just a single metallodielectric interface, but two, we create the metal-insulator-metal (MIM) waveguide shown schematically in Figure 1.4. The MIM geometry more significantly confines the electromagnetic fields in the dielectric region than a single metallodielectric surface [12]. As illustrated in Figure 1.4, an Ag/SiO$_2$/Ag waveguide with SiO$_2$ thicknesses of 30 nm "shrinks" light that in free space has a wavelength $\lambda_{\mathrm{air}} = 620$ nm down to a SP wavelength of $\lambda_{\mathrm{sp}} = 200$ nm. Thinner insulator thicknesses allow accessing even larger $k-$vectors or shorter wavelengths, $\lambda_{\mathrm{sp}} < \lambda_{\mathrm{air}}/10$. This was experimentally demonstrated in an Au/SiO$_2$/Au geometry by Miyazaki and Kurokawa [13].
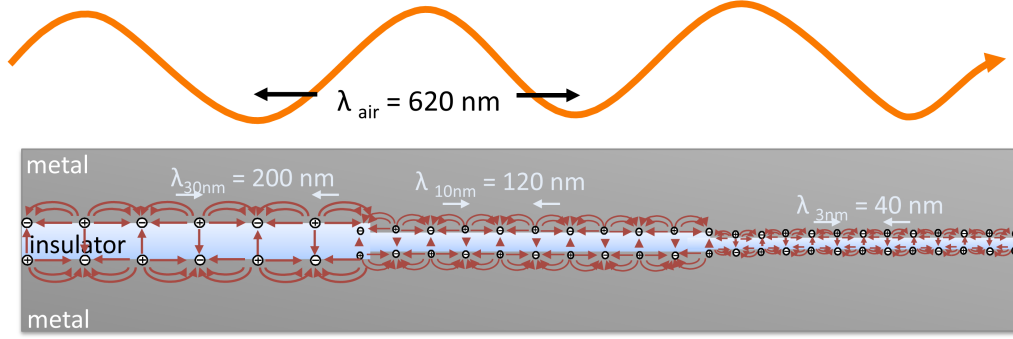
Figure 1.4. Top: a photon in free space at a wavelength of $\lambda_{\mathrm{air}} = 620$ nm, or an energy of 2 eV. Bottom: Inside a planar Ag-SiO$_2$-Ag metal-insulator-metal (MIM) waveguide, light of this same energy is sustained as surface plasmons with a much shorter wavelength λ_{sp}. For a 30 nm thick insulator, $\lambda_{\mathrm{sp}} = 200$ nm; 10 nm thick, $\lambda_{\mathrm{sp}} = 120$ nm; 3 nm thick, $\lambda_{\mathrm{sp}} = 40$ nm—less than 1/10 of the free-space wavelength.

1.4   Exciting Surface Plasmons

As illustrated by the dispersion diagram in Figure 1.3, there is a mismatch in the momentum between the surface plasmon and free-space photons at a given energy. Because of this, clever strategies must be devised to efficiently excite SPs with light. A number of geometries have been developed to achieve this, several of which are shown in Figure 1.5. First, a grating can be defined in the metal film with a periodic spacing Λ that matches the appropriate in-plane momentum of the SP, $k_x = k \sin \theta$, as shown in Figure 1.5b [10]. In this case, phase-matching is satisfied when $\beta = k \sin \theta + 2\pi m/\Lambda$, where m is an integer. The reverse process can also take place: surface plasmons propagating along a metal/dielectric interface with a grating can radiate into free space.

More generally, any subwavelength scatterer on the metal film, such as random surface roughness with dimension a_i, can be used to somewhat less efficiently couple free-space photons at a number of different $k-$vectors (Figure 1.5c). In this case, the phase-matching condition is $\beta = k \sin \theta + \Delta k$, where $\Delta k = 2\pi m/a_i$. Again, roughness
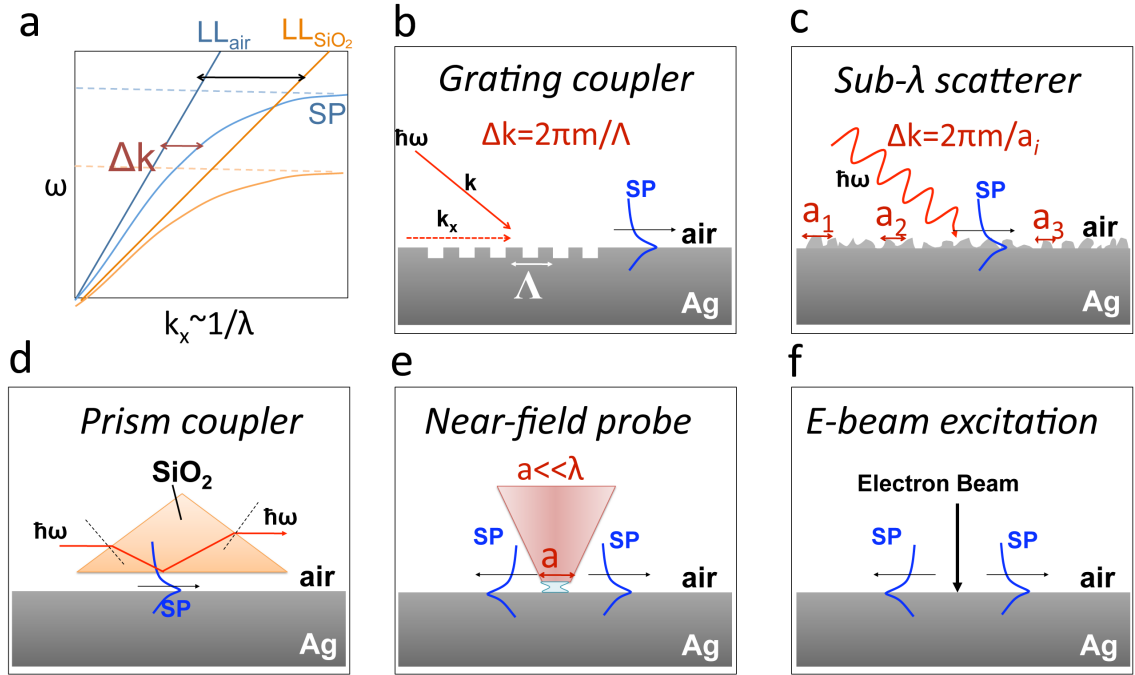
Figure 1.5. Methods of exciting surface plasmons at an Ag/air interface. (a) SP dispersion diagram (SP), showing the light line in air (LL_{air}, $\omega = ck$), the light line in SiO_2 (LL_{SiO_2}, $\omega = ck/n_{SiO_2}$, and the momentum mismatch Δk. A number of techniques have been developed to couple free-space photons into SPs at the Ag/air interface, such as (b) grating couplers, (c) subwavelength scatterers, (d) prism couplers, (e) near-field probes, and (f) electron-beam excitation. See text for details.

or designed localized scatterers can also be used to outcouple bound surface plasmons into free space.

Additionally, we can take advantage of total internal reflection inside a prism of refractive index n that differs from air, such as SiO_2. As indicated in Figure 1.5a, the light inside the prism has a wavevector that overlaps with a portion of the Ag/air SP dispersion relation. As shown in in Figure 1.5d, total internal reflection occurs at the prism/air interface, exciting surface plasmons by tunneling below to the Ag/air interface. This is known as the Otto configuration [14], and a similar geometry as the Kretschmann configuration [15].

A near-field probe with an aperture that is much much smaller than the wavelength of light can also be used to excite surface plasmons at much smaller length scales [16], as seen in Figure 1.5e. The subwavelength aperture $a << \lambda$ allows a number of wave vectors near the desired β, allowing phase-matched excitation of surface plasmons.

Alternatively, we desire methods of exciting surface plasmons that do not require incident photons. In Figure 1.5f, we consider a high-energy electron beam impinging on a metal surface that disturbs the equilibrium electron plasma in the metal, directly and locally exciting surface plasmons as the electrons at the surface of the metal oscillate (see [17] and references therein). This is the basis of cathodoluminescence spectroscopy as it applies to plasmonics, a technique utilized in Chapter 2 and Chapter 3 of this thesis.

1.5 Scope of This Thesis

This thesis is devoted to the investigation, both experimental and theoretical, of light emission in a number of plasmonic nanostructures. The first two chapters of this thesis present cathodoluminescence imaging spectroscopy as a new technique for characterizing surface plasmons on metal films and localized in nanocavity resonators, with experimental observations supported by analytical calculations and electromagnetic simulation.

In Chapter 2, we develop CL imaging spectroscopy as a tool for investigating

metallic films and nanostructures. This technique enables extremely localized surface plasmon excitation, a feature we exploit in both planar metal geometries and plasmonic nanocavities. We use CL to excite SPPs that propagate along an Ag or Au film, ultimately outcoupling via nanofabricated gratings, and from the emitted CL intensity determine the near-resonance SPP propagation distances. We also find good agreement between measured values and those expected from analytical calculations. Moreover, we demonstrate that CL can be used to excite localized SPs in a nanocavity geometry consisting of a semiconductor nanowire encapsulated in an Ag film. The incident electron beam excites both band-edge luminescence in the ZnO, as well as SP resonances of the Ag film.

We apply this same technique to excite and image modes in more complex resonator geometries in Chapter 3. The specific structure chosen is an annular nanoresonator, consisting of concentric grooves in a metal film that surround a flat plateau. Scanning the electron beam across the surface of the resonator yields cathodoluminescence emission that, when correlated with the excitation position, enables mapping the spatial variation of specific plasmonic modes. This analysis is performed in both Ag and Au resonators, and the experimental observations are supported by simulations of the electric field profiles of the modes, as well as calculations of the predicted CL emission.

The latter portion of this thesis is devoted to a specific plasmonic nanocavity geometry, the core-shell nanowire resonator. In Chapter 4, we embark on a theoretical investigation of the modes supported by the Si-Ag core-shell nanowire resonator. We find that this geometry sustains modes in structures with dimensions as small as $\lambda/50$. We also discuss the Purcell effect as it applies to plasmonic nanocavities, and demonstrate that the core-shell nanowire resonator can enhance the rate of spontaneous emission. Chapter 5 explains two routes to fabricating these structures, as well as methods we use to characterize their optical properties.

Chapter 6 considers active core-shell nanowire resonators that contain bright III-V semiconductor core materials. We design these structures such that the resonator mode dramatically enhances the rate of spontaneous emission at the emitting wave-

length of the active material, and calculate total decay rate enhancements above $8000\times$ the emission rate in free space. Furthermore, theory predicts that this geometry reorients the direction of far-field radiation, a feature crucial for designing on-chip, directional light-emitting diodes. Finally, Chapter 7 provides a thesis summary and outlook.